Available online at www.sciencedirect.com
ScienceDirect
International Journal of Thermal Sciences 48 (2009) 975–984
International Journal of Thermal Sciences
www.elsevier.com/locate/ijts

Flow emerging from annular-conical nozzle combinations and impinging onto a cylindrical cavity

S.Z. Shuja, B.S. Yilbas *, S.A. Khan

ME Department, KFUPM, Dhahran 31261, Saudi Arabia

Received 23 March 2008; received in revised form 11 June 2008; accepted 18 June 2008

Available online 23 July 2008

Abstract

Flow emerging from a combination of annular and conical nozzles and impinging onto a cylindrical cavity at elevated all temperature is considered, and the flow field and heat transfer rates from the cavity are computed. In the simulations, two cavity depths and four average jet velocities at nozzle exit are accommodated. Reynolds Stress Turbulence model is introduced to account for the turbulence. Air is used as working fluid while steel is considered as the cavity material. It is found that the Nusselt number attains high values in the neighborhood of the stagnation zone at the cavity bottom surface, which is more pronounced for 1 mm depth cavity.

Keywords: Jet impingement; Heat transfer; Cylindrical cavity

1. Introduction

Jet impingement is widely observed in process industry and one of the important applications of jet impingement is high power laser processing. The impinging jet influences the heat transfer rates from the irradiated field and prevents the heated surface from the high temperature oxidation reactions. Depending on the type of laser processing, assisting gas can be inert avoiding the chemical reactions and influences the heat transfer rates only at the impinging surface. This situation is observed for laser cutting of thin sheet metals, plastics, and ceramics. The impinging gas can assist the process through enhancing the material removal rate from the irradiated section while modifying the heat transfer rates from the surface. Assisting gas usually emerges from a nozzle, which is situated co-axially with the laser beam. Moreover, depending on the nozzle type and cavity shape formed in the workpiece by a laser beam, fluid structure and heat transfer rates from the cavity change. The nozzles used in the laser processing can be annular or conical. However, combination of annular and conical nozzles may result in improved heat transfer rates from the cavity surface. Consequently, investigation into the heat transfer rates from the cavity surface due to jet emerging from the annular and conical nozzle combination and impinging onto the cavity at elevated wall temperature becomes necessary.

Considerable research studies are carried out to examine jet impingement and heat transfer rates. Thermal performance of heat sinks with confined impinging jet was investigated by Li et al. [1]. They indicated that an appropriate impinging distance with the minimum thermal resistance could be found at a specific Reynolds number, and the optimal impinging distance increased as the Reynolds number increased. The heat transfer characteristics of turbulent round jet impinging on an inclined concave surface were examined by Lee et al. [2]. They showed that the displacement of the maximum Nusselt number from the stagnation point increased with increasing surface angle or decreasing nozzle-to-surface distance. Heat transfer due to laminar jet impingement onto an isothermal wall within one side closed long duct was examined by Dagtekin and Oztop [3]. They showed that the mean Nusselt number increased almost linearly with increasing Reynolds number at the isothermal surface. The velocity measurement in a turbulent impinging jet was carried out by Birch et al. [4]. They showed that the outer shear layer of the wall jet produced a mean flow field, which was essentially the same as a simple free shear layer.

* Corresponding author.
E-mail address: bsyilbas@kfupm.edu.sa (B.S. Yilbas).

1290-0729/$ – see front matter
doi:10.1016/j.ijthermalsci.2008.06.014

Nomenclature

H	enthalpy ..... K/kg
h	heat transfer coefficient ..... $W/m^2 K$
K	thermal conductivity
k	turbulent kinetic energy
L	length along cavity bottom ..... m
p	pressure
P	rate of production
R_{ij}	Reynolds stress
R_{ih}	energy generation due to Reynolds stress
Re	Reynolds no.
r	distance in the radial direction
t	time
T	temperature
u^*	friction velocity
U	arbitrary velocity
V	axial velocity component
$\forall$	volume
x	distance in the axial direction

Greek

α	thermal diffusivity
Γ	arbitrary diffusion coefficient
ε	energy dissipation
λ	turbulence intensity
μ	dynamic viscosity
ν	kinematic viscosity
ρ	density (function of temperature and pressure for gas)
τ	shear stress
σ	variable Prandtl no.
θ	nozzle cone angle
Φ	viscous dissipation
ϕ	arbitrary variable
Π	energy transport due to pressure excluding strain interactions
Π^w	energy transport due to wall reflection
Λ	energy transport by diffusion

Subscript

amb	ambient
i, j	arbitrary direction
jet	gas jet at inlet
l	laminar
max	maximum
p	a typical node in the computational grid
ref	reference
t	turbulent
v	viscous sublayer
w	wall

The non-linear flow and heat transfer dynamics of a slot jet impinging on a slightly curved concave surface were studied by Eren et al. [5]. They developed new correlations for local, stagnation point, and average Nusselt number as a function of jet Reynolds number and dimensionless circumferential distance. The numerical simulation of turbulent heat transfer in a plane impinging jet was carried out by Hattori and Nagano [6]. They indicated that the Nusselt number decreased monotonously in the wall-jet development direction. Multiple flow patterns and heat transfer in confined jet impingement were examined by Li et al. [7]. They showed that the flow patterns mainly depended on the Reynolds number, and the flow dynamics and thermal behaviors were similar in the stagnation region. The experimental and numerical investigation of a confined impinging air jet at high Reynolds numbers were carried out by Baydar and Ozmen [8]. They indicated that there exited a linkage among the sub-atmospheric region, turbulence intensity, and heat transfer; in addition, the predictions of standard k–ε turbulence model were in agreement with the experimental results except for the nozzle-to-plate spacing of less than one. Shuja et al. [9] investigated jet impingement onto a flat plate and heat transfer rates from the surfaces. They showed that nozzle configuration has significant effect on the heat transfer rates. Yilbas et al. [10,11] studies jet impingement onto cavities. They indicated that heat transfer rates changes around the cavity surface. However, the early studies [10,11] were limited with single nozzle (conical or annular) and, therefore, the extension of the early studies is necessary to include the influence of combination of annular and conical nozzles onto flow structure and heat transfer. Consequently, present study examines the flow field and heat transfer rates from the cylindrical cavity subjected to the impinging jet emerging from the combined nozzle consisting of annular and conical sections. The flow field and heat transfer rates are simulated numerically for two cavity depths and various average jet velocities at the nozzle exit. The cavity wall is kept at 1500 K to resemble the laser produced cavity. The Reynolds Stress Turbulence Model (RSM) is used to account for the turbulence.

2. Modeling of flow filed and heat transfer

In laser machining applications, an assisting gas jet is used. The assisting gas jet emerges from a nozzle and impinges onto the cavity surface in the workpiece. The cavity surface is almost at the melting temperature of the substrate material. The heat transfer rates from the cavity surface depend onto the nozzle geometry used and the cavity depth. The heat transfer rates from the surface influences the laser heating situation. Moreover, in the case of laser thick material processing, one of the nozzle types used is the annular nozzle [12]. Since the flow field associated with the gas jet emerging from the combination of annular and conical nozzles and impinging onto the cavity with elevated wall temperature is unique, the authors' could not find similar work in the open literature. Consequently, investigation into jet impingement and heat transfer rates from the cavity resembling the laser heating situation becomes essential. Jet emerging from a combination of annular and conical nozzles

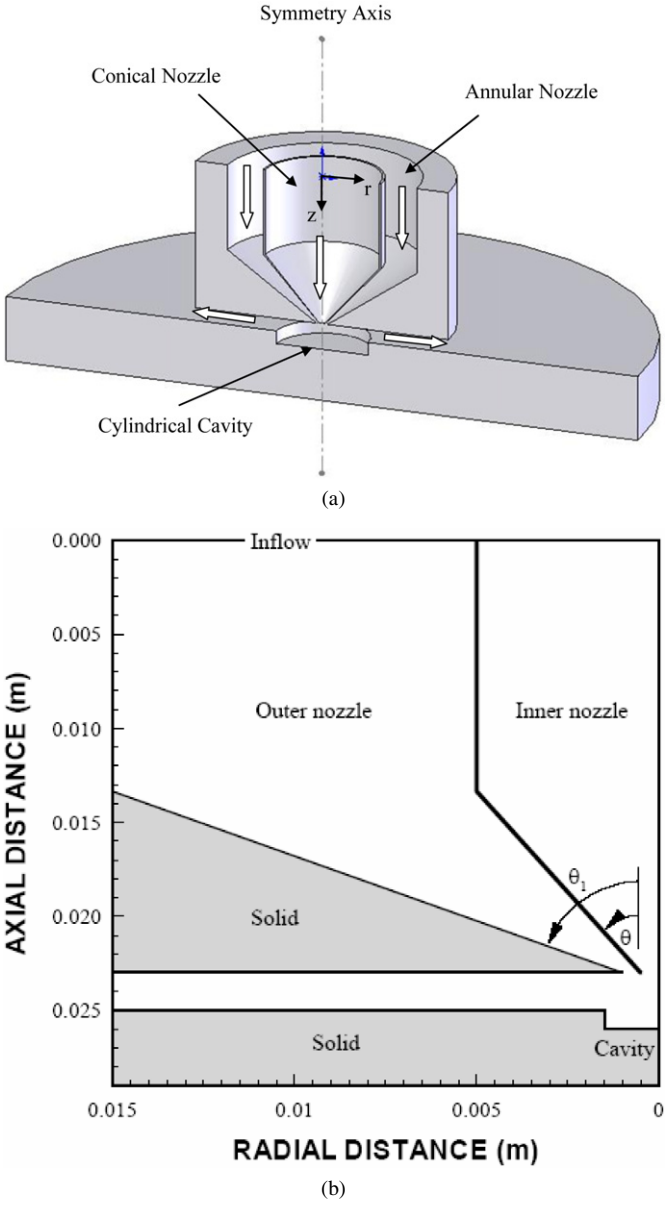

Fig. 1. (a) 3-Dimensional view of the combined nozzle and the cavity. (b) Geometrical configuration and solution domain of combined nozzle and the cylindrical cavity.

Table 1
Size and depth of the cylindrical cavity and cone angles of annular and conical nozzle combination (Fig. 1(b))

Cavity diameter (m)	Cavity depth (m)	Annular and conical nozzle angles	
		Inner angle ($\theta°$)	Outer angle ($\theta_1°$)
0.003	0.0005	40	55
0.003	0.001	40	70

and impinging onto a cylindrical cavity is considered. A constant elevated wall temperature is assumed at the cavity surface to resemble the laser produced cavity. The geometric arrangements of the annular and conical nozzle combination and the cavity are shown in Fig. 1 (a) and (b), while the nozzle and the cavity configurations are given in Table 1.

2.1. Conservation equations for the flow filed

The steady axisymmetric flow conditions with the compressibility and variable properties of the working fluid are considered to formulate the jet impingement onto the cylindrical cavity. The governing flow and energy equations can be written in the Cartesian tensor notation as:

(i) The continuity equation

$$\frac{\partial}{\partial x_i}(\rho U_i) = 0 \tag{1}$$

(ii) The momentum equation

$$\frac{\partial}{\partial x_i}(\rho U_i U_j) = \frac{\partial p}{\partial x_j} + \frac{\partial}{\partial x_i}\left[\mu\left(\frac{\partial U_i}{\partial x_j} + \frac{\partial U_j}{\partial x_i}\right) - \rho R_{ij}\right] \tag{2}$$

(iii) The energy equation

$$\frac{\partial}{\partial x_i}(\rho U_i H) = \frac{\partial}{\partial x_i}\left[\frac{\mu}{\sigma}\frac{\partial H}{\partial x_i} - \rho R_{ih}\right] \tag{3}$$

The flow field is turbulent; therefore, Reynolds stress turbulence model (RSM), which is based on the second-moment closure, is used in the analysis. The selection of the turbulence model is based on the previous study [13]; in which case, standard two equation models over estimates the turbulent kinetic energy generation in the stagnation region [14]. The transport equation of the Reynolds stress (R_{ij}) is

$$\frac{\partial}{\partial x_m}(U_m R_{ij}) = P_{ij} + \Lambda_{ij} - \varepsilon_{ij} + \Pi_{ij} + \Pi_{ij}^{w} \tag{4}$$

where $P, \Lambda, \varepsilon, \Pi$ and Π^w are the rate of production, transport by diffusion, rate of dissipation, transport due to turbulent pressure excluding strain interactions and transport due to wall reflection respectively. Eq. (4) consists of six partial differential equations; one for the transport of each of the six independent Reynolds stresses. The production term (P_{ij}), diffusion (Λ_{ij}), dissipation (ε_{ij}), transport due to turbulent pressure (Π_{ij}) and the modeling of the wall reflection (Π_{ij}^{w}) are referred to [15].

2.2. Flow boundary conditions

Four boundary conditions are considered in accordance with the geometric arrangement of the problem, as shown in Fig. 1(a).

2.2.1. Solid wall

For the solid wall, the no-slip condition is assumed at the solid wall, and the boundary condition for the velocity at the solid wall therefore is

$$U_i = 0 \tag{5}$$

2.2.2. Generalized wall functions for normal and shear turbulent stresses for the RSM model

When the flow is very near the wall, it undergoes a rapid change in direction; therefore, the wall-functions approach is

not successful in reproducing the details of the flow. Consequently the turbulent stresses and fluxes at the near-wall grid points are calculated directly from their transport equations. In this case, the near-wall region lying between the wall and the near-wall computational node at x_p can be represented by two layers: the fully viscous sublayer, defined by $Re_v = x_v\sqrt{k_v}/v \approx 20$, and a fully-turbulent layer. The wall shear stress near the wall is employed, i.e. $\overline{vw}|_{z_v} = \tau_w/\rho$, which serves as the boundary condition for the $\overline{vw}$ transport equation.

In relation to normal stresses, the turbulence energy must decrease quadratically towards a value of zero at the wall, therefore a zero-gradient condition for the normal stresses is physically realistic. This situation is insufficient to ensure an accurate numerical representation of near-wall effects. An improved approach for internal cells is needed in respect of evaluating volume integrated production and dissipation of normal stresses (these are normally evaluated at cell centers, using linear interpolation, and then multiplied by the cell volume). Considering $\overline{v}^2$ as an example, the volume-integrated production of $\overline{v}^2$ between the wall and the P-node may be approximated by,

$$\int_{\Delta r}\int_{0}^{z_p} P_{22}\,d\forall \cong \int_{\Delta r}\int_{x_v}^{x_p} -2\overline{vw}\frac{\partial V}{\partial x}\,d\forall = 2\tau_w\left(\frac{V_p - V_v}{x_p - x_v}\right)x_p\Delta r \tag{6}$$

where V_p and V_v follow from the log-law. No contribution arises from the viscous sublayer, since $\overline{vw} = 0$ in this layer. An analogous integration of the dissipation rate with the assumptions,

$$\varepsilon = \frac{2\nu k_v}{x_v^2} \qquad 0 \leqslant x \leqslant x_v$$

$$\varepsilon = \frac{C_\mu^{3/4}k_p^{3/2}}{\kappa x_v} \qquad x_v \leqslant x \leqslant x_p$$

leads to

$$\int_{\Delta r}\int_{0}^{x_p} \varepsilon\,d\forall \cong \left[\frac{2\nu k_p}{x_v} + \frac{C_\mu^{3/4}k_p^{3/2}}{\kappa}\ln\left(\frac{x_p}{x_v}\right)\right]\Delta r \tag{7}$$

an analogous treatment is applied to $\overline{v}^2$, while the production of $\overline{w}^2$ in the viscous and turbulent near wall layers region is zero.

The values resulting from Eqs. (6) and (7) are added, respectively, to the volume-integrated generation and dissipation computed for the upper half of the near-wall volume. It should be noted that for the wall-law approach, the near-wall dissipation (ε_p) is not determined from its differential equation applied to the near-wall cell surrounding the node. Instead, and in accordance with the log law, this value is obtained via the length scale from $\varepsilon_p = C_\mu^{3/4}k_p^{3/2}/\kappa z_p$, which serves as the boundary conditions for inner cells.

2.2.3. Inlet conditions

The boundary conditions for temperature and the mass flow rate at the combined nozzle inlet are introduced. Therefore, at the nozzle inlet: mass flow rate is specified and altered giving the mean jet velocities at the nozzle exit 25, 50, 75, and 100 m/s. In addition, temperature is specified, i.e. $T =$ specified (300 K). The selection of the values of the mean velocities is due to the gas jet velocities, in general, used in laser gas assisted processing. It should be noted that the flow is compressible and introducing the velocity profile at the combined nozzle inlet is inappropriate due to the density variation; consequently, mass flow inlet is introduced.

The values of k and ε are not known at the nozzle inlet, but can be determined from the turbulent kinetic energy i.e.

$$k = \lambda\bar{u}^2 \tag{8}$$

where $\bar{u}$ is the average inlet velocity and λ is a percentage.

The dissipation is calculated from $\varepsilon = C_\mu k^{3/2}/aD$, where D is the diameter. The values $\lambda = 0.03$ and $a = 0.005$ are commonly used and may vary slightly in the literature [16]. The turbulence is assumed to be isotropic at the inlet such that:

$$\overline{u_i u_j} = 0$$

$$\overline{u_i u_i} = \frac{2}{3}k, \quad \text{no summation over the index } i$$

2.2.4. Outlet

The flow is considered to be extended over a long domain; therefore, the boundary condition (outflow boundaries, Fig. 1(b)) for any variable ϕ is

$$\frac{\partial\phi}{\partial x_i} = 0 \tag{9}$$

where x_i is the normal direction at outlet.

2.2.5. Symmetry axis

At the symmetry axis, the radial derivative of the variables is set to zero, i.e.

$$\frac{\partial\phi}{\partial r} = 0 \tag{10}$$

except for

$$V = \overline{vw} = \overline{vh} = \overline{wh} = 0 \tag{11}$$

2.3. Solid side

2.3.1. Constant wall temperature boundary

Two constant temperature boundaries are considered. The first one is in the radial direction far away from the symmetry axis at a constant temperature $T = T_{\text{amb}}$ (300 K). It should be noted that the constant temperature boundary condition is set at different locations in the radial directions. The boundary condition ($T =$ constant) located in the radial direction had no significant effect on the temperature and flow field in the stagnation region. Therefore, this boundary condition is set for a radial distance of 0.015 m from the symmetry axis. The second constant temperature boundary is set at the cavity walls (as shown in Fig. 1(a)) at $T =$ constant (1500 K).

2.3.2. Solid fluid interface

The coupling of conduction within the solid and convection within the fluid, termed conjugation, is required for the present analysis at the solid fluid interface. The appropriate boundary conditions are continuity of heat flux and temperature and are termed boundary conditions of the fourth kind, i.e.

$$T_{w_{\text{solid}}} = T_{w_{\text{gas}}} \quad \text{and} \quad K_{w_{\text{solid}}} \frac{\partial T_{w_{\text{solid}}}}{\partial x} = K_{w_{\text{gas}}} \frac{\partial T_{w_{\text{gas}}}}{\partial x} \tag{12}$$

No radiation loss from the solid surface is assumed due to the small surface area of the cavity.

The heat transfer coefficient is determined from:

$$h = \frac{(-K_{w_{\text{solid}}}(\partial T_{w_{\text{solid}}}/\partial n))}{(T_{w_{\text{gas}}} - T_{\text{ref}})} \tag{13}$$

where $(\partial T_{w_{\text{solid}}}/\partial n)$ is the temperature gradient in the solid normal to the cavity surface while T_{ref} is the reference temperature and equals to the jet temperature at the nozzle exit. The local Nusselt number is:

$$Nu = \frac{hL}{K_{\text{gas}}}$$

where L is length along the cavity bottom.

The wall shear stress is determined from the rate of fluid strain at the cavity wall, which is:

$$\tau = \mu\left(\frac{\partial V}{\partial n}\right) \tag{14}$$

where $(\partial V/\partial n)$ is the rate of fluid strain at the cavity wall and n represents the direction normal to the cavity surface.

2.4. Gas properties

The equation of state is used and variable properties of air are accommodated in the simulations.

3. Numerical method and simulation

A control volume approach is employed to discretize the governing equations. The discretization procedure is given in the literature [17]. The problem of determining the pressure and satisfying continuity may be overcome by adjusting the pressure field so as to satisfy continuity. A staggered grid arrangement is used in which the velocities are stored at a location midway between the grid points, i.e. on the control volume faces. All other variables including pressure are calculated at the grid points. This arrangement gives a convenient way of handling the pressure linkages through the continuity equation and is known as Semi-Implicit Method for Pressure-Linked Equations (SIMPLE) algorithm. The details of this algorithm are given in the literature [17].

The computer program used for the present simulation can handle a non-uniform grid spacing. In each direction fine grid spacing near the gas jet impinging point and the cavity is allocated while gradually increased spacing for locations away from the cavity is considered. Elsewhere the grid spacing is adjusted to maintain a constant ratio of any of two adjacent spacing. The number of grid planes used normal to the x and r directions are 220 and 272, respectively, in the simulations. The grid independence tests were conducted and it is observed that the grid selected results in the grid-independent solution. The grid sizes used for the grid independent tests and resulting in the percentage variation of the maximum velocity magnitude along the symmetry axis is 0.1%.

Nine variables are computed at all grid points; these are: two velocity components, local pressure, five turbulence quantities and the temperature.

4. Results and discussion

Jet emerging from the annular conical nozzle combination and impinging onto a cylindrical cavity is considered. The influence of the average jet velocity (V_j) exiting the nozzle and depth of the cavity on flow field and heat transfer rates is examined. The geometric configuration of nozzle is kept the same in the simulations.

Fig. 2 shows normalized velocity (V/V_j) contours in the cavity and in the region of the nozzle exit for different nozzle exit average velocity and two depths of the cavity. Flow emerging from the conical and annular nozzle merges without forming a significant shear layer between the jets. However, jet emerging from a conical nozzle (inner nozzle, Fig. 1(a)) influences the radial expansion of the annular nozzle (outer nozzle, Fig. 1(b)). This results in a complex flow structure in the region of the jet outer boundary. In this case, a steep streamline curvature is observed in the region above the cavity edge, which is more pronounced for the shallow cavity (depth = 0.5 mm). However, the radial acceleration of the impinging jet upon leaving the cavity is observed for the sallow cavity (depth = 0.5 mm). This is because of the pressure buildup in the cavity and small penetration depth of impinging jet into the cavity because of the small cavity depth (shallow cavity). Consequently, flow developed between the impinging jet outer boundary and the boundary of the radial jet emanating from the cavity results in circulation in this region. Moreover, increasing the impinging jet average velocity at the nozzle exit influences the flow field around the cavity. This is more pronounced for the shallow cavity. In this case, increasing impinging jet velocity enhances the radial acceleration of the flow emanating from the cavity. The flow expansion around the cavity edge, due to sharp edges, contributes to the radial acceleration flow emanating from the cavity.

Fig. 3 shows pressure coefficient $(\Delta P/\frac{1}{2}\rho V_j^2)$ in the close region of nozzle exit and the cavity for two cavity depths and four average impinging jet velocities at the nozzle exit. Pressure coefficient increases with increasing velocity in the region close to the cavity bottom. This is because of the penetration of the impinging jet into the cavity, which in turn results in high pressure region close to the cavity bottom wall. In the case of the shallow cavity (depth = 0.5 mm), the kinetic energy of the impinging jet is not totally dissipated in the cavity due to radial acceleration towards the cavity exit. This results in shallow pressure region in the cavity bottom region. Increasing jet velocity alters the pressure coefficient slightly in the cavity. This is more pronounced for the deep cavity (depth = 1 mm).

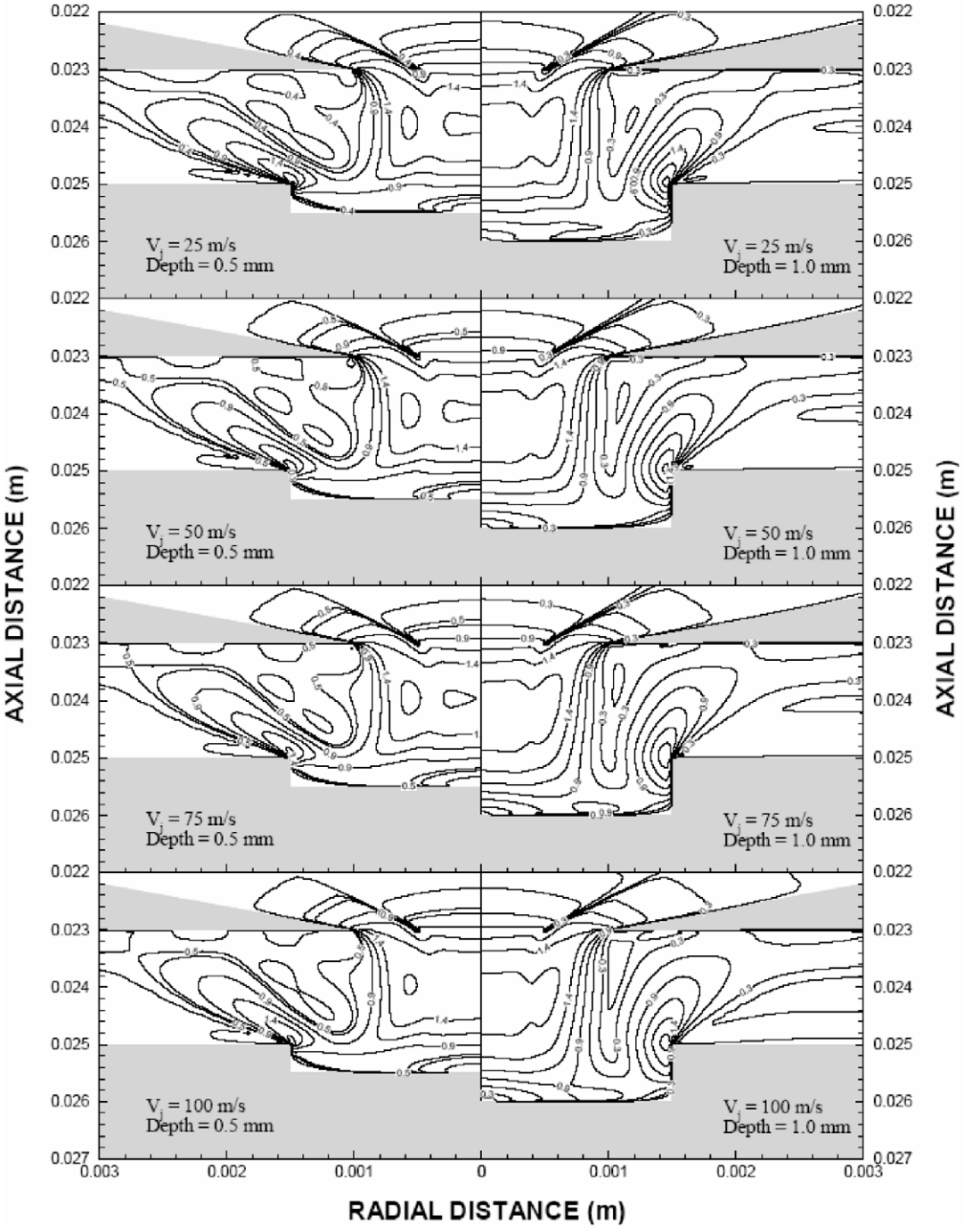

Fig. 2. Normalized velocity magnitude (V/V_j, V_j is the average velocity at the nozzle exit) contours in the region of nozzle exit and the cavity.

The thermodynamic pressure developed in the vicinity of the cavity wall contributes to the pressure buildup in the cavity. It should be noted that the cavity wall is assumed to be at elevated temperature (1500 K) to resemble the laser heating situation. Consequently, convective heat transfer from the cavity wall to the fluid enhances the gas pressure and temperature in the vicinity of the cavity wall. The formation of the circulation cell in the neighborhood of the impinging jet and the radial jet emanating from the cavity is evident for the shallow cavity; in which case, the constant pressure contours forms the complete circle. In this case of the deep cavity, the size of the circulation cell is relatively smaller than that corresponding to the shallow cavity. The development of the large circulation cell is because of the radially accelerated jet, which emanates from the cavity. The flow developed due to the shear between the impinging jet outer boundary and the boundary of the radial jet emanating from the cavity is responsible for the large circulation cell formation.

Fig. 4 shows normalized temperature contours (T/T_j) in the region close to the nozzle exit and in the cavity for two cavity depths and four average jet velocities at the nozzle exit. Temperature profile changes with the cavity depth. Jet penetration into the cavity enhances with increasing the cavity depth. This

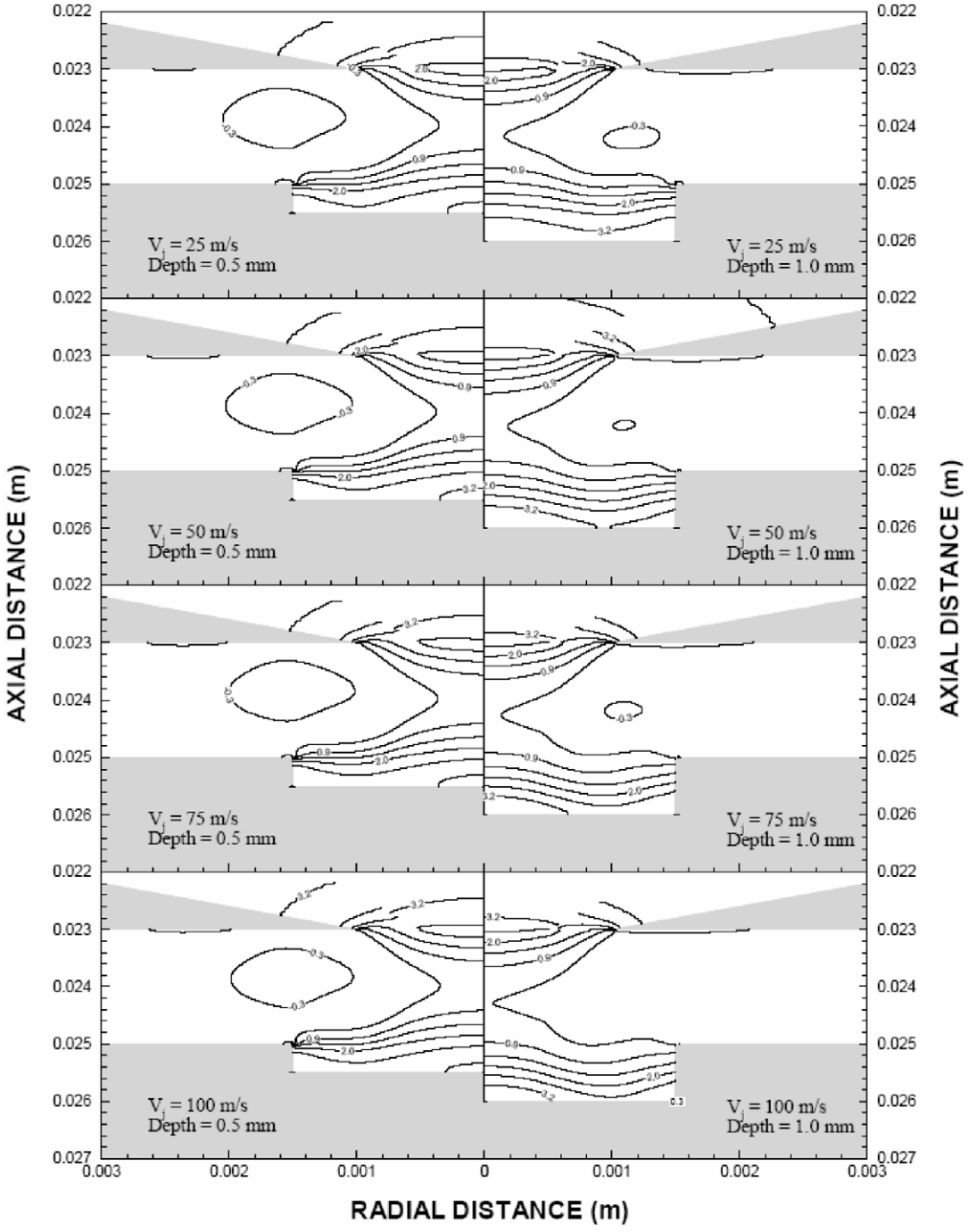

Fig. 3. Pressure coefficient contours in the region of nozzle exit and the cavity.

modifies temperature distribution in the cavity. Moreover, the effect of jet velocity on temperature distribution in the cavity is not significant, provided that some small effects are visible from the temperature contours. The small effect of jet velocity on temperature contours in the cavity is associated with the convective and conduction heating of the fluid by the cavity walls. It should be noted that the cavity wall temperature is kept constant at 1500 K during the simulations. However, the radial acceleration of the jet emanating from the shallow cavity suppresses the thermal boundary layer thickness around the cavity edge. The thermal boundary layer thickens in the region of the cavity wall, because of the convective and conduction heating as well as the stagnation pressure buildup around the cavity wall. This is particularly true at the cavity wall bottom. Moreover, increasing jet velocity reduces the thermal boundary layer thickness around the side wall of the cavity. In this case, the radial acceleration of the flow in the cavity exit region is responsible for thinning the boundary layer in this region.

Fig. 5 shows the Nusselt number variation along the cavity bottom for different jet velocities at nozzle exit and two cavity depths. It should be noted that the distance 0 m represents the cavity edge while 0.0014 m represents the cavity center.

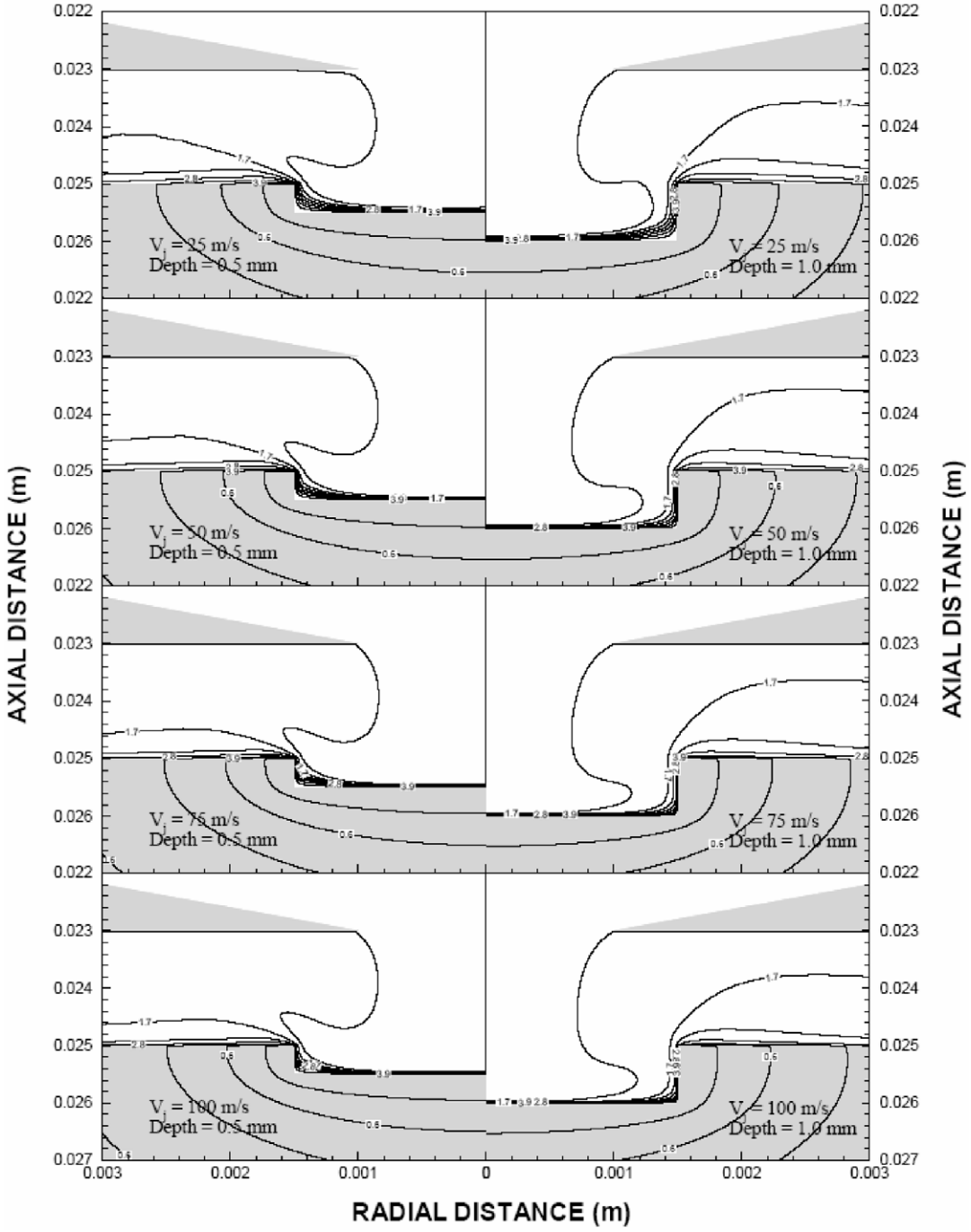

Fig. 4. Normalized temperature (T/T_j, T_j is jet temperature at the nozzle exit) contours in the region of nozzle exit and the cavity.

The Nusselt number increases with increasing jet velocity at the nozzle exit. This is more pronounced at the cavity edge where the radial acceleration of the flow emanating from the cavity enhances the heat transfer rates from the cavity bottom. Heat transfer rate reduces to almost zero at the cavity center due to the stagnation region developed, which in turn results in considerably low Nusselt number. In addition, the thermodynamic pressure developed in the boundary layer next to the cavity bottom suppresses the heat transfer from the cavity wall. The Nusselt number increases sharply in the vicinity of the stagnation region, which is particularly true for the deep cavity. The sharp increase in the Nusselt number is associated with the pressure differential developed across the stagnation zone and its neighborhood. Consequently, flow acceleration due to pressure differential in this region is responsible for the sharp increase in the heat transfer coefficient. However, the side walls of the cavity suppress the flow acceleration in the cavity resulting in reduced heat transfer rates and the Nusselt number. This situation is observed lightly for the shallow cavity; in which case, radial acceleration of the flow is not suppressed considerably by the cavity side walls. As a consequence, a radial jet

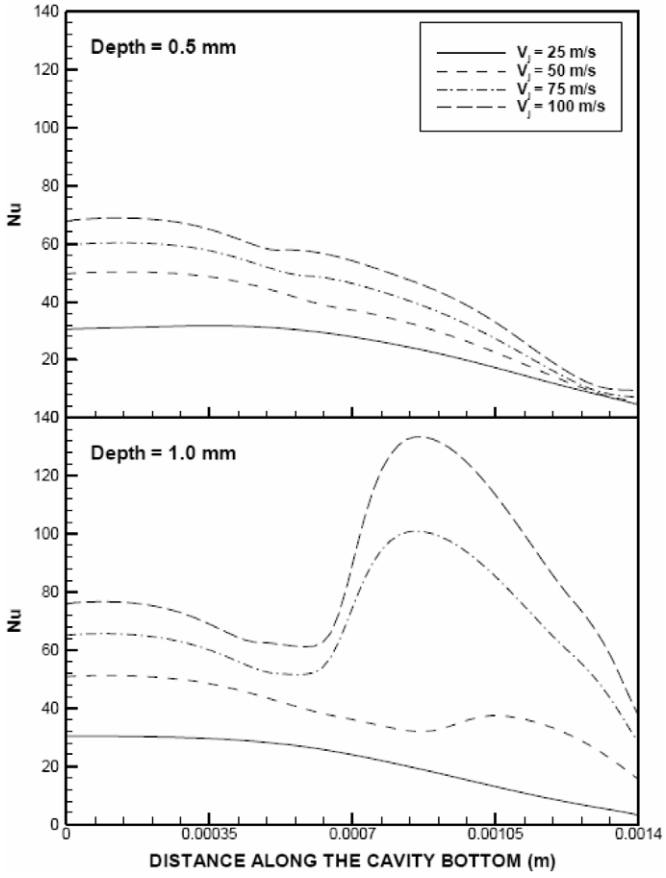

Fig. 5. Nusselt number along the cavity wall for two cavity depths and different average jet velocities at the nozzle exit.

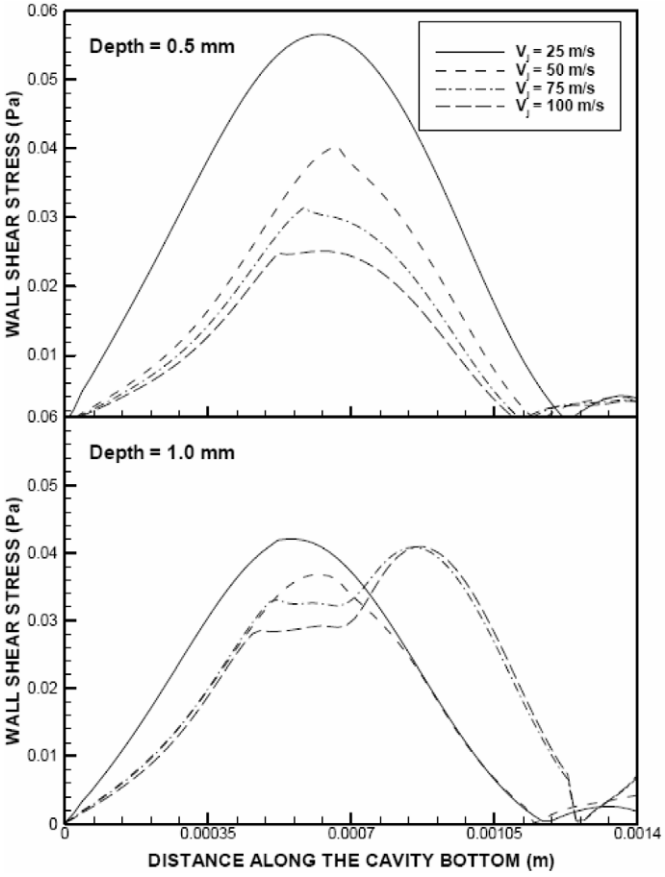

Fig. 6. Wall shear stress along the cavity wall for two cavity depths and different average jet velocities at the nozzle exit.

is formed, which emanates from the cavity enhancing the heat transfer rates and the Nusselt number in this region.

Fig. 6 shows the wall shear stress along the cavity wall for different average jet velocities at the nozzle exit and two cavity depths. It should be noted that the distance 0 m represents the cavity edge while 0.0014 m corresponds to the cavity center. The shear stress reduces in the region of the cavity center due to the stagnation zone. However, it increases sharply reaching its maximum in the neighborhood of the stagnation zone. This is because of the attainment of the high rate of fluid strain due to radial acceleration of the flow in this region. The location of the maximum shear stress at the cavity bottom changes with the mean jet velocity at the nozzle exit. This is more pronounced for the deep cavity (depth = 1.0 mm). Consequently, increasing averaged jet velocity influences the flow structure in the cavity. Moreover, wall shear stress reduces slightly for the deep cavity (depth = 1.0 mm). This because of the rate of fluid strain in the region of the cavity bottom, which becomes small for the deep cavity due to the small radial acceleration in the bottom region of the cavity.

5. Conclusions

The jet emerges from a combined nozzle, including annular and conical nozzles, and impinges onto a cylindrical cavity with elevated wall temperature is examined. The flow field and heat transfer rates are simulated for four average velocities at the nozzle exit and two cavity depths. It is found that a radial jet is developed emerging from the cavity due to pressure differential developed between the stagnation zone and its neighborhood. The streamline curvature affect contributes to the radial acceleration of the jet emerging from the cavity, which is more pronounced for the shallow cavity. The Nusselt number attains high values in the region next to the stagnation zone at the cavity bottom, which is particularly true for the deep cavity. In this case, the radial acceleration of the flow occurs due to the pressure differential developed in this region. The Nusselt number attains higher values for the deep cavity than that corresponding to the shallow cavity. Moreover, increasing average jet velocity at the nozzle exit enhances significantly the Nusselt number due to increased convective cooling. The wall shear stress reduces significantly at the cavity bottom, provided that it increases when the radial acceleration enhances the rate of fluid strain in the cavity wall. The wall shear stress attains slightly higher values for shallow cavity as compared to the deep cavity.

Acknowledgements

The authors acknowledge the support of King Fahd University of Petroleum and Minerals, Dhahran, Saudi Arabia, for this work.

References

[1] H. Li, S. Chao, G. Tsai, Thermal performance measurement of heat sinks with confined impinging jet by infrared thermography, Int. J. Heat Mass Transfer 48 (2005) 5386–5394.

[2] C.H. Lee, K.B. Lim, S.H. Lee, Y.J. Yoon, N.W. Sung, A study of the heat transfer characteristics of turbulent round jet impinging on an inclined concave surface using liquid crystal transient method, Exp. Therm. Fluid Sci. 31 (2007) 559–565.

[3] I. Dagtekin, H.F. Oztop, Heat transfer due to double laminar slot jets impingement onto an isothermal wall within one side closed long duct, Int. Comm. Heat Mass Transfer 35 (2008) 65–75.

[4] A.D. Birch, R.P. Cleaver, M. Fairweather, G.K. Hargrave, Velocity and concentration field measurements in a turbulent, impinging flammable jet, Chem. Engrg. Sci. 60 (2005) 219–230.

[5] H. Eren, N. Celik, B. Yesilata, Nonlinear flow and heat transfer dynamics of a slot jet impinging on a slightly curved concave surface, Int. Comm. Heat Mass Transfer 32 (2006) 364–371.

[6] H. Hattori, Y. Nagano, Direct numerical simulation of turbulent heat transfer in plane impinging jet, Int. J. Heat Fluid Flow 25 (2004) 749–758.

[7] X. Li, J.L. Gaddis, T. Wang, Multiple flow patterns and heat transfer in confined jet impingement, Int. J. Heat Fluid Flow 26 (2005) 746–754.

[8] E. Baydar, Y. Ozmen, An experimental and numerical investigation on a confined impinging air jet at high Reynolds numbers, Appl. Therm. Engrg. 25 (2005) 409–421.

[9] B.S. Yilbas, S.Z. Shuja, M.O. Budair, Influence of conical and annular nozzle geometric configurations on flow and heat transfer characteristics due to flow impingement onto a flat plate, Numer. Heat Transfer, Part A 48 (2005) 917–939.

[10] B.S. Yilbas, S.Z. Shuja, M.O. Budair, Jet impingement onto a cavity, Int. J. Numer. Methods Heat Fluid Flow 12 (2002) 817–838.

[11] B.S. Yilbas, S.Z. Shuja, M.O. Budair, Jet impingement onto a conical cavity with elevated wall temperature, Int. J. Numer. Methods Heat Fluid Flow 14 (8) (2004) 1011–1028.

[12] United States Patent 5220149.

[13] S.Z. Shuja, B.S. Yilbas, M.O. Budair, Gas jet impingement on a surface having a limited constant heat flux area—various turbulence models, Numer. Heat Transfer, Part A 36 (2) (1999) 171–200.

[14] T.J. Craft, L.J.W. Graham, B.E. Launder, Impinging jet studies for turbulence model assessment. II. An examination of the performance of four turbulence models, Int. J. Heat Mass Transfer 36 (1993) 2685–2697.

[15] W.C. Lasher, D.B. Taulbee, Reynolds stress model assessment using round jet experimental data, Internat. J. Heat Fluid Flow 15 (5) (1994) 357–363.

[16] D. Elkaim, M. Reggio, R. Camarero, Simulating two-dimensional turbulent flow by using the k–ε model and the vorticity-stream function formulation, Int. J. Numer. Methods Fluids 14 (1992) 961–980.

[17] S.V. Patankar, Numerical Heat Transfer, McGraw-Hill, New York, 1980.